The Mass of the Central Black Hole in the Seyfert Galaxy NGC 3783

Christopher A. Onken & Bradley M. Peterson
Department of Astronomy, The Ohio State University, Columbus, OH 43210
onken, peterson@astronomy.ohio-state.edu

ABSTRACT

Improved analysis of ultraviolet and optical monitoring data on the Seyfert 1 galaxy NGC 3783 provides evidence for the existence of a supermassive, $(8.7\pm1.1)\times10^6$ $M_\odot$, black hole in this galaxy. By using recalibrated spectra from the *International Ultraviolet Explorer* satellite and ground-based optical data, as well as refined techniques of reverberation mapping analysis, we have reduced the statistical uncertainties in the response of the emission lines to variations in the ionizing continuum. The different time lags in the emission line responses indicate a stratification in the ionization structure of the broad-line region and are consistent with the virial relationship suggested by the analysis of similar active galaxies.

Subject headings: galaxies: active — galaxies: individual (NGC 3783) — galaxies: nuclei — galaxies: Seyfert —- ultraviolet: galaxies

1. INTRODUCTION

The primary model that has emerged over the last few decades for the radiation source of an active galactic nucleus (AGN) is accretion onto a supermassive black hole (SMBH). Variations in the ionizing continuum have been seen to influence the strength of emission lines arising from the broad-line region (BLR). Cross-correlation of the continuum and emission line light curves yields a characteristic time lag with which each line echoes the continuum fluctuations (Blandford & McKee 1982). This reverberation mapping technique has been used to measure the sizes of BLRs for a growing number of AGNs (see Wandel, Peterson, & Malkan 1999; Kaspi et al. 2000).

In addition to the BLR size, reverberation analysis can be used to estimate the mass of the SMBH. The reliability of these reverberation masses has been debated because of the uncertainty surrounding the common assumption of virialized BLR gas motions. The detailed kinematics and structure of the BLR is an unresolved issue and could lead to systematic errors on the order of a factor of a few or perhaps more (see Fromerth & Melia 2001; Krolik 2001). However, the excellent agreement between the black hole mass-bulge velocity dispersion (M-σ) relationships for reverberation-mapped AGNs and normal galaxies (Ferrarese et al. 2001) suggests the systematic discrepancy introduced in reverberation mapping is small. Additionally, AGNs for which multiple emission lines have been mapped (NGC 5548, 3C 390.3, NGC 7469) show an inverse relationship between the time lag and the emission line width, consistent with the gas motions being dominated by the gravity of the SMBH (Peterson & Wandel 1999, 2000).

A combined optical and UV monitoring campaign was carried out on the Seyfert 1 galaxy NGC 3783 by the *International AGN Watch* consortium, making use of the *International Ultraviolet Explorer* (*IUE*), the *Hubble Space Telescope*, and a host of ground-based observatories over a period of 7 months in 1991-1992. The results of that work have been published by Reichert et al. (1994), Stirpe et al. (1994), and Alloin et al. (1995). Compared to the consortium's earlier study of another Seyfert galaxy, NGC 5548 (see Clavel et al. 1991; Peterson et al. 1991; Dietrich et al. 1993), the

emission-line time lags were relatively uncertain, too poorly constrained in fact to reveal any possible virial relationship between line width and time lag.

The continued rarity of such campaigns, however, makes it clearly desirable to learn as much as possible from the extant datasets. This provides the motivation for our current study.

With the release of an updated processing pipeline and calibration for *IUE* data, the possibility arose to re-analyze the spectra of NGC 3783 and reduce the uncertainties of the emission-line time lags. In addition, the techniques of reverberation analysis have matured in the years since the original data were published, now providing more consistent methodology for cross-correlation and error estimation. Thus, we have re-examined the data, deriving more precise results for the emission line reverberation and revising the previous estimates of the reverberation mass.

The next section describes the observations and how the data were reduced (§2). In §3 we explain the analysis procedure and give our cross-correlation results. Section 4 discusses the results and the SMBH mass determination, and our conclusions are summarized in §5.

2. OBSERVATIONS AND DATA REDUCTION

2.1. UV Data

The *IUE* observations of NGC 3783 were conducted in 69 separate epochs, with two sampling rates. The first interval (of 45 epochs) had an average spacing of 4.0 days, while the final 24 epochs observed the AGN with an average spacing of 2.0 days. A more complete description of the UV observing program is provided by Reichert et al. (1994).

In addition to the original *IUE* Spectral Image Processing System (IUESIPS), Reichert et al. (1994) used a Gaussian extraction method (GEX; see Clavel et al. 1991) to obtain the spectra of NGC 3783. After the original data had been taken, a new standard processing pipeline was introduced. The main advantages of the New Spectral Image Processing System (NEWSIPS; Nichols et al. 1993) with respect to the older IUESIPS are the improved photometric accuracy and higher S/N of the spectra; these characteristics have been achieved by introducing a new method of raw data science registration (which both reduces the fixed pattern noise in the images and improves the photometric corrections), a weighted slit extraction method, and re-derived absolute flux calibrations. NEWSIPS also includes corrections for non-linearity that might have affected previous studies. Overall, NEWSIPS-processed spectra show average S/N increases of 10–50% over IUESIPS data (Nichols & Linsky 1996).

We retrieved the NEWSIPS-extracted short wavelength prime camera (SWP; Harris & Sonneborn 1987) spectra from the *IUE Final Archive*[1]. While Reichert et al. (1994) analyzed data from both the SWP and long wavelength prime cameras, we have limited our study to observations made with the SWP instrument, which has a wavelength range of 1150–1975 Å in the low-dispersion mode (Newmark et al. 1992).

Each spectrum was examined and several types of problems led to spectra being removed from further consideration: (1) low S/N (determined by inspection, but corresponding roughly to a continuum S/N limit of 10); (2) unusual spectral features (possibly due to grazing cosmic-ray impacts); (3) short exposure times (when longer-exposure data were available from the same epoch and the line flux data were discrepant). Some anomalous features were checked against the GEX frames, from which cosmic ray impacts were carefully removed. Problems with the spectra were ignored in cases where they occurred in spectral regions outside those used in computing line and continuum fluxes. Continuum and emission line flux values were measured using the wavelengths limits listed in Table 1.

The continuum was defined by a linear fit through four spectral regions (1340–1370 Å, 1440–1480 Å, 1710–1730 Å, and 1840–1860 Å). An alternate fit through the first three of these regions produced consistent results. Wavelength-specific problems in two cases (SWP 45150, SWP 45206) led us to substitute the alternate continuum fit for these spectra.

We have estimated the flux uncertainties by considering instances in which multiple independent exposures were obtained at the same epoch

[1] http://ines.laeff.esa.es/ines/

(i.e., a single pointing toward the target). Flux ratios between pairs of points within each epoch were calculated and the standard deviation of the flux ratios was taken as the fractional uncertainty for all observations. This analysis was conducted independently for each emission line and continuum band. As noted above, however, highly discrepant data were removed prior to this analysis. In spite of our use of an edited dataset, the large number of data pairs contributing to our error estimate (about 35) justifies our continued use of these values in the analysis. The final UV dataset is given in Table 2 for the continuum measurements and in Table 3 for the emission lines.

The velocity width desired for the reverberation mass calculation is related to the emission line velocity full width at half-maximum (V_{FWHM}) by

$$\sigma = \frac{\sqrt{3}V_{FWHM}}{2}, \tag{1}$$

where the factor of $\sqrt{3}/2$ is used to maintain consistency with previous work (e.g., Wandel et al. 1999; Kaspi et al. 2000) and assumes isotropic gas motion.

An RMS spectrum was created from the data to isolate the varying parts of the emission lines and it was from this spectrum that the primary V_{FWHM} values for the emission lines were measured. The V_{FWHM} data were constructed by considering the extreme flux values within the continuum regions, fitting two continuum slopes (to the highest flux levels and lowest flux levels), and averaging the measures of V_{FWHM} derived from the two continuum determinations. Finally, the data were converted to their rest-frame widths using $z = 0.009730 \pm 0.000007$ (Theureau et al. 1998). Previous work examining the difference between using the mean and RMS spectra have not produced significantly different results (e.g., Kaspi et al. 2000), but in principle the RMS spectrum should better trace the gas with which we are concerned. We have measured line widths from both spectra (Figure 1) and report the results of our mean and RMS V_{FWHM}^{rest} measurements in Table 4. Geocoronal Lyα emission blended into the Lyα spectral region precludes V_{FWHM} measurement for this line and thus also prevents Lyα contribution to the mass determination, but cross-correlation analysis is still feasible by excluding the contaminated portion of the spectrum (see Table 1).

2.2. Optical Data

Ground-based optical spectroscopy was conducted over the same time period as the *IUE* observations. The optical data analyzed here were retrieved from the *AGN Watch* website[2], and details of the observations are described by Stirpe et al. (1994). We have limited our investigation to the data gathered at the Cerro Tololo Inter-American Observatory (CTIO) 1.0 m telescope to ensure the most homogeneous dataset possible for the cross-correlation analysis and for the construction of the mean and RMS spectra. Spectra that were excessively noisy or contained other anomalies were discarded from consideration, leaving 37 CTIO observations for further analysis.

Narrow spectral lines are assumed not to vary over the timescales these data are probing. Thus the individual spectra were scaled to a constant flux by using the spectral scaling technique of van Groningen & Wanders (1992). This method computes a smooth scaling function between the input spectrum and a reference (the mean spectrum in this case, shown in Figure 2) over a specified wavelength range. We scaled over the spectral region 4972–5150 Å in order to span the redshifted [O III] $\lambda\lambda$4959, 5007 emission lines and a suitable amount of continuum. We found that two iterations were required for full convergence. This reduced the fractional RMS scatter in the [O III] λ5007 light curve (measured between 5028 and 5090 Å) to less than 2.5%. Additional iterations failed to produce any light curves with smaller scatter. The mean [O III] λ5007 flux was normalized to 8.44×10^{-13} erg s^{-1} cm^{-2}, the value derived by the careful analysis of Stirpe et al. (1994).

Following the calibration of the spectra, the Hβ line was measured between 4830 and 4985 Å (with the continuum set by a linear fit between 4800–4820 Å and 5130–5150 Å). The flux uncertainties were measured in the same way as for the UV data (§2.1), and the results are given in Table 5. Due to the smaller optical dataset, the flux errors for Hβ and the 5150 Å continuum rely on only seven data pairs. To be cautious, we have been more conservative in our estimation of the optical flux uncertainties. The method for measuring V_{FWHM}^{rest} was

[2] http://www.astronomy.ohio-state.edu/~agnwatch/

also applied to the optical data and yielded values of $(2.91\pm0.19)\times10^3$ km s^{-1} for the RMS spectrum and $(2.65\pm0.02)\times10^3$ km s^{-1} for the mean optical spectrum.

3. LIGHT CURVE ANALYSIS

In Table 6 we compare the sampling characteristics of our data with the previously published light curves. When we bin the data in each epoch, the variability parameters of the old and new UV datasets appear nearly identical. The "excess variance", F_{var}, represents the mean fractional variation of each dataset (see Rodrígues-Pascual et al. 1997); R_{max} is the ratio of maximum to minimum flux levels. The updated optical dataset is much more sparse than the previously published data because of our desire for the most homogeneous dataset possible.

Figure 3 shows the light curves for each of the UV and optical emission lines and continuum bands. Applying the techniques described by Peterson et al. (1998), we generated cross-correlation functions (CCFs) relating the various emission line light curves to the 1355 Å continuum flux. We report both peak (τ_{peak}) and centroid (τ_{cent}) cross-correlation lags. However, the reader should be warned that "lags" in the text will hereafter refer to centroids, unless otherwise noted, and that such lags do not represent a simple phase shift between the light curves.

As Koratkar & Gaskell (1991a) noted for NGC 3783 (and other reverberation-mapped AGNs), the choice of what threshold to use for the centroid calculation can significantly affect the resulting time lag. Figure 4 shows that some lines tend toward larger lags and others toward smaller values as the centroid becomes increasingly dominated by the peak value. For the interpolated CCF (ICCF; Gaskell & Peterson 1987; White & Peterson 1994), we experimented with different interpolation lengths and different thresholds for the calculation of the lag centroid. Our subsequent analysis uses an interpolation unit of 0.1 days in both light curves (interpolating one dataset at a time, with the resulting lags averaged) and a centroid threshold of 80% of the peak correlation coefficient.

In addition to the ICCF, we calculated the discrete correlation function (DCF; Edelson & Krolik 1988) for each continuum band and emission line. While the DCF, which requires binning of the data, is more likely to miss a real correlation than the ICCF under poor sampling conditions, it is also less likely to introduce a spurious relationship (White & Peterson 1994). Gaskell (1994) notes that the DCF also relies on interpolation, but does so in the correlation function, rather than the original time series. The ICCF and DCF methods have been compared by various authors (e.g., White & Peterson 1994; Litchfield, Robson, & Hughes 1995) and typically yield similar results.

To assess the uncertainties in the time lag calculations, we used the Monte Carlo (MC) methods of Peterson et al. (1998). This technique for model-independent error estimation consists of two components, each testing for a separate contribution to the cross-correlation uncertainty. To account for the uncertainty in an individual flux measurement, each data point in the light curve is altered by a random Gaussian deviation that corresponds to the quoted flux error (calculated by the method described in §2.1). The result of many such realizations, referred to as "flux randomization" (FR), should yield average values equal to the original data with standard deviations given by the original uncertainties. Secondly, the effects of non-uniform temporal sampling of the AGN fluctuations are investigated with "random subset selection" (RSS). Given a sample of N observations, N data points are randomly chosen from the set (ignoring whether they have been chosen previously). While DCF and ZDCF (Alexander 1997) analyses can weight multiply-selected data, the ICCF (which we use for our MC calculations) does not consider the flux uncertainties and simply excludes the redundant data points. Ignoring these data reduces the set by $\sim N/e$ on average and so should yield a wider range of peak lags from the ICCF. Repeated MC realizations (at least 10^3 in the present work; combining the FR/RSS methods for each calculation) are used to create a cross-correlation peak distribution (CCPD; Maoz & Netzer 1989), which provides an empirical measurement of the uncertainties for both τ_{cent} and τ_{peak}.

3.1. Emission Lines

The light curves for each emission line (He II $\lambda1640$ + O III] $\lambda1663$, Si IV $\lambda1400$ + O IV] $\lambda1402$,

Lyα, C IV λ1549, Si III] λ1892 + C III] λ1909, and Hβ) were run through the ICCF, DCF, and FR/RSS programs, using the 1355 Å continuum data as the "driving" light curve. The CCFs and CCPDs are shown for each emission line in the panels of Figure 5. The CCPDs are shown to give a graphical indication of the empirical uncertainties and are scaled to the maximum value in each panel.

Each of the emission lines was very well correlated with the continuum flux. The poorest correlation with the continuum was found for Si III] λ1892 + C III] λ1909, which was found to have a peak ICCF value of r_{max}=0.354 (i.e., a probability of arising from an uncorrelated parent population of roughly < 0.001) and we limited the range of computation for this line to $\pm$16 days to avoid aliasing. Table 7 summarizes the previous data and our new results.

Our results for the UV emission lines are generally in agreement with those of Reichert et al. (1994). It should be noted, however, that the peak and centroid lags calculated by Reichert et al. (1994) and Stirpe et al. (1994) used the 1460 Å continuum as the driving light curve. The results quoted here are consistent with those derived from the recalibrated data with the continuum centered at 1460 Å rather than at 1355 Å. Because of the large uncertainties assigned to previous lag values, most of our NEWSIPS lags are within 1-σ of the old data. The exceptions are Si III] λ1892 + C III] λ1909, for which the IUESIPS-based data failed to produce any lag at all, and Hβ. The GEX extraction method yielded a peak lag for Si III] λ1892 + C III] λ1909 similar to what we found, but a centroid lag approximately 2-σ larger than the current result. Our centroid lag for Hβ was only slightly more than 1-σ greater than the previous value.

The significant discrepancy between our Hβ results and those of Wandel et al. (1999, $4.5^{+3.6}_{-3.1}$ days) arises from the double-peaked nature of the CCF. The centroid lag calculated for the 5150 Å continuum-Hβ CCF is based on fewer points than the 1355 Å continuum-Hβ lag, and gives precedence to the peak at smaller lags. We have greater confidence in the results that use the UV continuum data, and those results closely match the UV-Hβ correlation found by Stirpe et al. (1994).

3.2. Continuum

Strong evidence for wavelength-dependent continuum lags has been found for only two AGNs (NGC 7469 and Akn 564), but appears to be consistent with simple accretion disk models that predict $\tau \propto \lambda^{4/3}$ (see Wanders et al. 1997; Collier et al. 1998, 2001). However, Korista & Goad (2001) note that diffuse emission from broad-line clouds can produce a similar wavelength dependence, so the origin of this phenomenon is not clear.

The large uncertainties still present in the NEWSIPS continuum lags prevent us from reasonably testing the τ–λ relationship because the continuum-continuum time lags we find are not statistically significant (see Table 7).

4. IMPLICATIONS FOR THE BLR AND THE SMBH

As the tabular data indicate, the expected pattern of more highly ionized lines having smaller time lags (i.e., originating closer to the ionization source) is reconfirmed by our analysis.

Figure 6 plots $V^{rest}_{FWHM}(RMS)$ versus τ^{rest}_{cent} for the five emission lines we measured. The virial assumption predicts a slope of -0.5 (in log-log space). Deviation from this relationship would contradict our model, but agreement with the predicted slope cannot rule out other dynamical possibilites (see Krolik 2001, and references therein).

The statistical problem of fitting to intrinsically scattered data with heteroscedastic errors has been addressed with computational methods by Akritas & Bershady (1996). However, our data has the additional difficulty of asymmetric errors in the lags. To account for the asymmetric time lag uncertainties we first used the larger of the two lag errors and then assessed in which direction the data points differed from the regression. We recalculated the fit using the errors toward the previous regression and confirmed that those were the appropriate choices in the final fit. The slope of the $V^{rest}_{FWHM}(RMS)$-τ^{rest}_{cent} relation derived by the regression software[3] was -0.450 ± 0.070, consistent with our expectations for a virial relationship (irrespective of the specific multiplicative factor relating the line widths and V_{FWHM} values). Hence, we fixed the slope at -0.5 and calculated the mass

[3] available at http://www.astro.wisc.edu/~mab/archive/stats/stats.html

independently for each emission line, applying our previously stated assumption of isotropic BLR gas motion and inserting the appropriate rest-frame values into the following equation:

$$M = \frac{3\ c\ \tau\ V_{FWHM}^2}{4\ G}. \quad (2)$$

Weighting the data by the uncertainty in the direction of the mean (since the lag errors are still asymmetric) yields an average SMBH mass of $(8.7{\pm}1.1){\times}10^6$ $M_\odot$.

Previous work with *IUE* archival data having much poorer temporal resolution measured a much larger C IV $\lambda1549$ time lag and derived a mass of $7.3^{+3.5}_{-3.6} \times 10^7$ $M_\odot$ (Koratkar & Gaskell 1991a,b). Wandel et al. (1999) calculated the Hβ lag with respect to the 5100 Å continuum from the light curves of Stirpe et al. (1994) and then used the RMS velocity width to estimate a mass of $1.1^{+1.1}_{-1.0} \times 10^7$ $M_\odot$. Applying this method to our version of the optical data yields an SMBH mass of $6.2^{+4.7}_{-6.1} \times 10^6 M_\odot$, within the 1-$\sigma$ error bars for our mass measurement with the full dataset. Fromerth & Melia (2000) employed a different means of measuring the velocity dispersion from the data of Reichert et al. (1994) and derived masses of $1.6^{+0.8}_{-0.4} \times 10^7$ $M_\odot$ and $1.3^{+0.8}_{-0.5} \times 10^7$ $M_\odot$ from Lyα and C IV $\lambda1549$, respectively. Various disk accretion models predicting a SMBH mass in the range of 2.0–7.0$\times10^7$ $M_\odot$ were cited by Alloin et al. (1995). However, they note the simple nature of these spatially thin, optically thick disk models and the potential for a large discrepancy from the true SMBH mass.

5. SUMMARY

We have conducted reverberation mapping analysis on recalibrated *IUE* and ground-based optical observations of the Seyfert 1 galaxy NGC 3783 with the goal of revising the mass estimate for the central SMBH. The NEWSIPS spectra confirm the existence of varying time lags for emission lines of different ionization potentials and provide a better constraint on the SMBH mass under the assumption of virial gas motion. The emission line time lags vary from 1.3 to 10.4 days, and analysis of peak and centroid time lags yield similar results for each line. Our mass determination revises the previous values to a mass of $(8.7{\pm}1.1){\times}10^6$ $M_\odot$.

We gratefully acknowledge support for this work through NASA grant NAG5-8397. C. A. O. thanks The Ohio State University for support through the Distinguished University Fellowship. We also thank Patrizia Romano for acquiring the NEWSIPS data, and Matthew A. Bershady for making available his statistical software. This research has made use of the NASA/IPAC Extragalactic Database (NED) which is operated by the Jet Propulsion Laboratory, California Institute of Technology, under contract with the National Aeronautics and Space Administration.

REFERENCES

Akritas, M. G. & Bershady, M. A. 1996, ApJ, 470, 706

Alexander, T. 1997, in Astronomical Time Series, ed. D. Maoz, A. Sternberg, & E. M. Leibowitz (Dordrecht: Kluwer), 163

Alloin, D., et al. 1995, A&A, 293, 293

Blandford, R. D., & McKee, C. F. 1982, ApJ, 255, 419

Clavel, J., et al. 1991, ApJ, 366, 64

Collier, S. J., et al. 1998, ApJ, 500, 162

Collier, S., et al. 2001, ApJ, 561, 146

Dietrich, M., et al. 1993, ApJ, 408, 416

Edelson, R. A., & Krolik, J. H. 1988, ApJ, 333, 646

Ferrarese, L., Pogge, R. W., Peterson, B. M., Merritt, D., Wandel, A., & Joseph, C. L. 2001, ApJ, 555, L79

Fromerth, M. J., & Melia, F. 2000, ApJ, 533, 172

Fromerth, M. J., & Melia, F. 2001, in ASP Conf. Ser. 224, Probing The Physics Of Active Galactic Nuclei By Multiwavelength Monitoring, ed. B. M. Peterson, R. S. Polidan, & R. W. Pogge (San Francisco: ASP), 377

Gaskell, C. M. 1994, in ASP Conf. Ser. 69, Reverberation Mapping Of The Broad-Line Region In Active Galactic Nuclei, ed. P. M. Gondhalekar, K. Horne, & B. M. Peterson (San Francisco: ASP), 111

Gaskell, C. M., & Peterson, B. M. 1987, ApJS, 65, 1

Harris, A. W., & Sonneborn, G. 1987, in Exploring the Universe with the *IUE* Satellite, ed. Y. Kondo (Dordrecht: Reidel), 729

Kaspi, S., Smith, P. S., Netzer, H., Maoz, D., Jannuzi, B. T., & Giveon, U. 2000, ApJ, 533, 631

Koratkar, A. P., & Gaskell, C. M. 1991a, ApJS, 75, 719

Koratkar, A. P., & Gaskell, C. M. 1991b, ApJ, 370, L61

Korista, K. T., & Goad, M. R. 2001, in ASP Conf. Ser. 224, Probing The Physics Of Active Galactic Nuclei By Multiwavelength Monitoring, ed. B. M. Peterson, R. S. Polidan, & R. W. Pogge (San Francisco: ASP), 411

Krolik, J. H. 2001, ApJ, 551, 72

Litchfield, S. J., Robson, E. I., & Hughes, D. H. 1995, A&A, 300, 385

Maoz, D., & Netzer, H. 1989, MNRAS, 236, 21

Newmark, J. S., Holm, A. V., Imhoff, C. L., Oliverson, N. A., Pitts, R. E., & Sonneborn, G. 1992, *IUE Observing Guide*, NASA *IUE* Newsletter, 47, 1

Nichols, J. S., Garhart, M. P., De La Peña, M. D., & Levay, K. L. 1993, *International Ultraviolet Explorer New Spectral Image Processing System Information Manual: Low-Dispersion Data, Version 1.0*, CSC/SD-93/6062

Nichols, J. S., & Linsky, J. L. 1996, AJ, 111, 1

Peterson, B. M., et al. 1991, ApJ, 368, 119

Peterson, B. M., & Wandel, A. 1999, ApJ, 521, L95

Peterson, B. M., & Wandel, A. 2000, ApJ, 540, L13

Peterson, B. M., Wanders, I., Horne, K., Collier, S., Alexander, T., Kaspi, S., & Maoz, D. 1998, PASP, 110, 660

Reichert, G. A., et al. 1994, ApJ, 425, 582

Rodríguez-Pascual, P. M., et al. 1997, ApJS, 110, 9

Stirpe, G. M., et al. 1994, ApJ, 425, 609

Theureau, G., Bottinelli, L., Coudreau-Durand, N., Gouguenheim, L., Hallet, N., Loulergue, M., Paturel, G., & Teerikorpi, P. 1998, A&AS, 130, 333

van Groningen, E., & Wanders, I. 1992, PASP, 104, 700

Wandel, A., Peterson, B. M., & Malkan, M. A. 1999, ApJ, 526, 579

Wanders, I., et al. 1997, ApJS, 113, 69

White, R. J., & Peterson, B. M. 1994, PASP, 106, 879

This 2-column preprint was prepared with the AAS LaTeX macros v5.0.

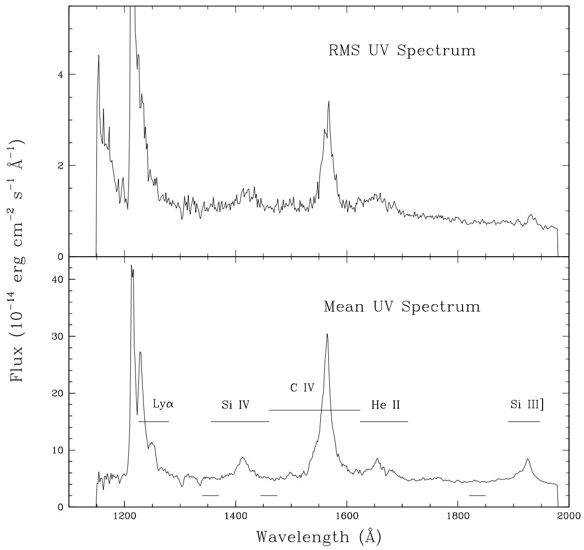

Fig. 1.— *Top*: RMS UV spectrum. *Bottom*: Mean UV spectrum. Wavelengths delineated above the spectrum indicate emission-line ranges; those below the spectrum mark ranges of continuum flux measurement.

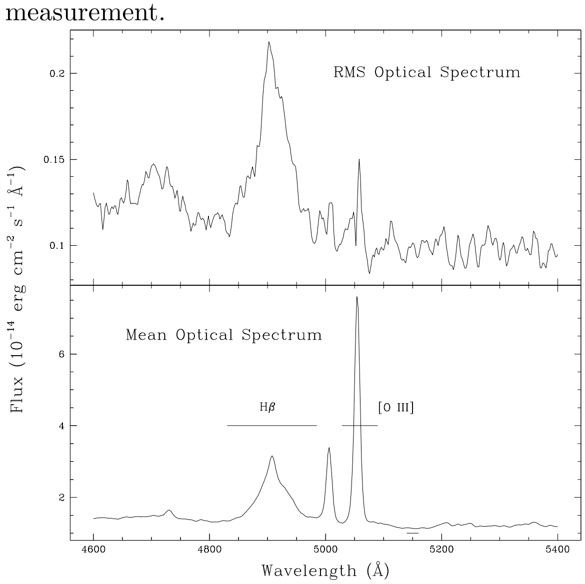

Fig. 2.— *Top*: RMS optical spectrum. *Bottom*: Mean optical spectrum. Wavelength indications as in Fig. 1.

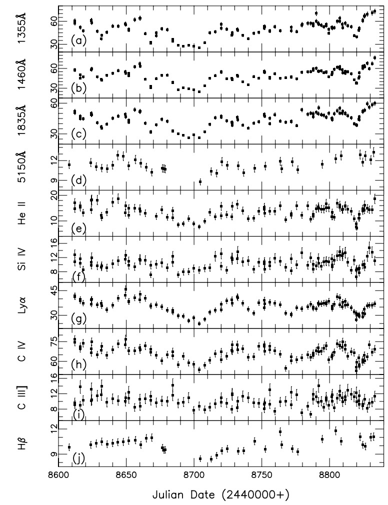

Fig. 3.— UV and optical light curves: (a) 1355 Å continuum, (b) 1460 Å continuum, (c) 1835 Å continuum, (d) 5150 Å continuum, (e) He II $\lambda1640$ + O III] $\lambda1663$, (f) Si IV $\lambda1400$ + O IV] $\lambda1402$, (g) Lyα, (h) C IV $\lambda1549$, (i) Si III] $\lambda1892$ + C III] $\lambda1909$, and (j) Hβ. Continuum fluxes are in units of 10^{-15} ergs cm^{-2} s^{-1} Å^{-1}. Emission line fluxes are given in units of 10^{-13} ergs cm^{-2} s^{-1}.

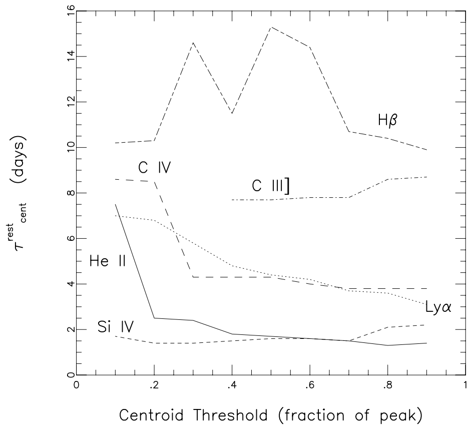

Fig. 4.— Rest-frame centroid time lag versus threshold level for centroid determination (as a fraction of the peak correlation coefficient). The data plotted are for He II $\lambda1640$ + O III] $\lambda1663$ (solid), Si IV $\lambda1400$ + O IV] $\lambda1402$ (short dashed), Lyα (dotted), C IV $\lambda1549$ (long dashed), Si III] $\lambda1892$ + C III] $\lambda1909$ (dot-short dashed), and Hβ (dot-long dashed).

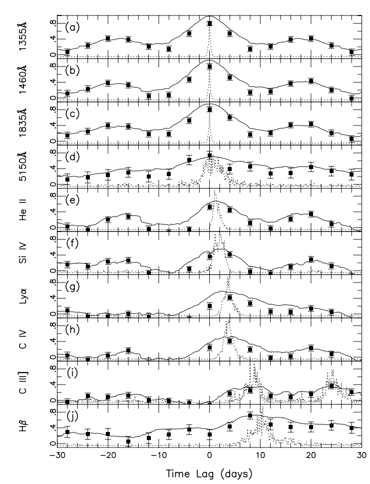

Fig. 5.— Results of cross-correlation of the 1355 Å continuum with (a) itself; (b) 1460 Å continuum; (c) 1835 Å continuum; (d) 5150 Å continuum; (e) He II $\lambda1640$ + O III] $\lambda1663$; (f) Si IV $\lambda1400$ + O IV] $\lambda1402$; (g) Lyα; (h) C IV $\lambda1549$; (i) Si III] $\lambda1892$ + C III] $\lambda1909$; (j) Hβ. The solid lines show the ICCFs, the data points are the DCFs, and the dashed lines represent the CCPDs. Note that the y-axis scale for the CCPDs is the fraction of MC realizations producing a centroid of that lag value and is scaled to the maximum in each panel.

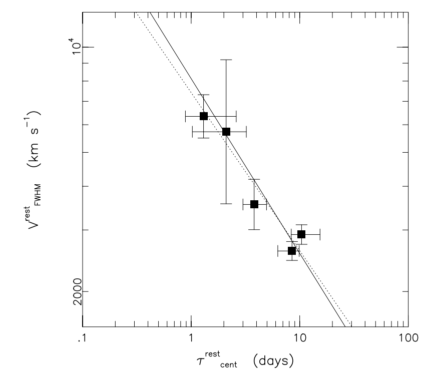

Fig. 6.— Rest-frame velocity FWHM versus rest-frame centroid time lag for the five emission lines we have measured. The dashed line is the best fit to the data; the solid line is the best fit with fixed slope of -0.5.

Table 1
Wavelength Limits

Line/Band	Wavelength Range (Å)
1355 Å continuum	1340–1370
1460 Å continuum	1445–1475
1835 Å continuum	1820–1850
5150 Å continuum	5140–5160
Lyα	1225–1280
Si IV λ1400 + O IV] λ1402	1355–1460
C IV λ1549	1460–1624
He II λ1640 + O III] λ1663	1624–1710
Si III] λ1892 + C III] λ1909	1890–1948
Hβ	4830–4985

Table 2

UV Continuum Flux Data[a]

Image Name	Julian Date (2,440,000+)	F(λ1355)	F(λ1460)	F(λ1835)
SWP 43438	8611.948	60.811±2.432	57.899±2.142	52.244±1.776
SWP 43439	8612.031	57.353±2.294	57.395±2.124	50.582±1.720
SWP 43472	8615.949	51.984±2.079	50.204±1.858	47.259±1.607
SWP 43473	8616.029	51.979±2.079	45.407±1.680	45.024±1.531
SWP 43485	8618.118	47.391±1.896	47.043±1.741	44.713±1.520
SWP 43539	8624.202	60.846±2.434	58.123±2.151	48.605±1.653
SWP 43540	8624.294	61.371±2.455	58.173±2.152	50.031±1.701
SWP 43541	8624.385	58.033±2.321	59.779±2.212	48.735±1.657
SWP 43557	8628.595	46.814±1.873	47.146±1.744	40.850±1.389
SWP 43587	8631.680	36.975±1.479	43.277±1.601	37.136±1.263
SWP 43588	8631.765	41.661±1.666	42.163±1.560	35.594±1.210
SWP 43636	8635.688	45.680±1.827	49.405±1.828	39.628±1.347
SWP 43676	8639.862	53.819±2.153	52.490±1.942	45.264±1.539
SWP 43716	8643.948	53.593±2.144	56.866±2.104	47.434±1.613
SWP 43871	8649.367	56.758±2.270	55.327±2.047	48.963±1.665
SWP 43872	8649.454	55.680±2.227	52.634±1.947	46.580±1.584
SWP 43894	8651.756	49.667±1.987	48.990±1.813	43.264±1.471
SWP 43895	8651.855	48.352±1.934	52.337±1.936	41.435±1.409
SWP 43921	8656.130	61.961±2.478	62.436±2.310	53.664±1.825
SWP 43945	8660.040	64.188±2.568	67.311±2.491	51.531±1.752
SWP 43946	8660.121	63.656±2.546	63.607±2.353	52.300±1.778
SWP 43962	8664.048	43.983±1.759	43.716±1.617	40.467±1.376
SWP 43995	8668.022	32.648±1.306	30.813±1.140	31.508±1.071
SWP 43996	8668.115	31.491±1.260	32.760±1.212	32.328±1.099
SWP 44020	8672.106	40.887±1.635	44.671±1.653	38.755±1.318
SWP 44048	8676.272	44.897±1.796	49.399±1.828	44.148±1.501
SWP 44072	8680.310	50.035±2.001	49.829±1.844	42.224±1.436
SWP 44099	8684.199	49.072±1.963	38.191±1.413	33.057±1.124
SWP 44100	8684.275	36.331±1.453	39.336±1.455	32.631±1.109
SWP 44126	8688.228	33.912±1.356	27.773±1.028	30.118±1.024
SWP 44149	8692.216	28.542±1.142	30.410±1.125	28.579±0.972
SWP 44176	8695.910	27.667±1.107	29.197±1.080	26.109±0.888
SWP 44189	8699.713	28.465±1.139	27.397±1.014	29.131±0.990
SWP 44208	8703.723	27.708±1.108	24.374±0.902	26.402±0.898
SWP 44237	8707.871	25.508±1.020	33.736±1.248	31.970±1.087
SWP 44267	8711.731	32.335±1.293	45.001±1.665	39.240±1.334
SWP 44307	8715.612	44.933±1.797	49.245±1.822	45.781±1.557
SWP 44349	8719.932	46.150±1.846	55.077±2.038	47.230±1.606
SWP 44350	8720.020	56.100±2.244	54.303±2.009	46.392±1.577
SWP 44381	8724.004	50.768±2.031	44.383±1.642	42.641±1.450
SWP 44408	8727.967	49.801±1.992	44.960±1.664	41.495±1.411

Table 2—*Continued*

Image Name	Julian Date (2,440,000+)	F(λ1355)	F(λ1460)	F(λ1835)
SWP 44409	8728.068	42.096±1.684	43.414±1.606	38.242±1.300
SWP 44410	8728.168	45.123±1.805	43.196±1.598	40.839±1.389
SWP 44434	8731.946	43.086±1.723	49.410±1.828	46.087±1.567
SWP 44435	8732.205	49.680±1.987	48.115±1.780	43.598±1.482
SWP 44461	8735.946	48.231±1.929	39.557±1.464	38.632±1.313
SWP 44486	8739.990	41.475±1.659	35.484±1.313	35.752±1.216
SWP 44492	8744.129	37.318±1.493	47.640±1.763	40.569±1.379
SWP 44581	8747.874	44.276±1.771	45.235±1.674	41.850±1.423
SWP 44627	8751.845	45.411±1.816	55.741±2.062	47.994±1.632
SWP 44628	8751.950	51.002±2.040	53.867±1.993	48.992±1.666
SWP 44629	8752.056	53.204±2.128	54.219±2.006	47.375±1.611
SWP 44659	8755.872	52.803±2.112	46.318±1.714	45.237±1.538
SWP 44660	8755.949	47.175±1.887	44.828±1.659	40.003±1.360
SWP 44682	8759.702	47.448±1.898	51.934±1.922	48.939±1.664
SWP 44731	8763.559	52.863±2.115	44.915±1.662	42.596±1.448
SWP 44760	8767.535	47.646±1.906	45.992±1.702	41.306±1.404
SWP 44803	8771.689	47.353±1.894	47.380±1.753	41.833±1.422
SWP 44804	8771.772	52.010±2.080	46.543±1.722	42.305±1.438
SWP 44830	8775.633	46.666±1.867	44.004±1.628	38.184±1.298
SWP 44873	8779.607	54.715±2.189	54.094±2.001	53.352±1.814
SWP 44907	8783.948	56.424±2.257	54.764±2.026	49.191±1.672
SWP 44918	8785.949	57.362±2.294	55.285±2.046	50.312±1.711
SWP 44921	8787.786	57.131±2.285	57.471±2.126	49.797±1.693
SWP 44922	8787.864	56.597±2.264	59.267±2.193	46.567±1.583
SWP 44935	8790.113	54.404±2.176	60.190±2.227	50.947±1.732
SWP 44949	8791.769	60.256±2.410	55.655±2.059	49.797±1.693
SWP 44950	8791.857	70.247±2.810	55.465±2.052	55.578±1.890
SWP 44964	8793.963	57.656±2.306	56.226±2.080	48.742±1.657
SWP 44974	8795.768	56.318±2.253	53.796±1.990	48.098±1.635
SWP 44992	8797.448	54.836±2.193	53.977±1.997	46.297±1.574
SWP 44993	8797.538	52.793±2.112	54.654±2.022	46.258±1.573
SWP 45010	8799.460	54.291±2.172	47.346±1.752	50.123±1.704
SWP 45024	8801.764	55.805±2.232	50.718±1.877	45.454±1.545
SWP 45025	8801.887	49.579±1.983	54.021±1.999	43.688±1.485
SWP 45026	8801.996	44.498±1.780	52.914±1.958	44.756±1.522
SWP 45038	8803.458	52.139±2.086	58.489±2.164	49.668±1.689
SWP 45052	8805.543	50.742±2.030	61.563±2.278	52.663±1.791
SWP 45063	8807.520	51.641±2.066	59.254±2.192	50.333±1.711
SWP 45064	8807.603	51.587±2.063	62.612±2.317	54.971±1.869
SWP 45081	8809.509	59.759±2.390	57.843±2.140	50.158±1.705
SWP 45082	8809.601	60.228±2.409	53.138±1.966	51.993±1.768

Table 2—*Continued*

Image Name	Julian Date (2,440,000+)	F(λ1355)	F(λ1460)	F(λ1835)
SWP 45096	8811.493	63.860±2.554	55.395±2.050	49.903±1.697
SWP 45097	8811.595	56.369±2.255	52.657±1.948	50.072±1.702
SWP 45106	8813.384	51.571±2.063	54.998±2.035	47.810±1.626
SWP 45118	8816.028	57.179±2.287	51.851±1.918	45.563±1.549
SWP 45133	8818.024	57.305±2.292	42.796±1.583	39.882±1.356
SWP 45150	8819.700	54.163±2.167	37.296±1.380	···
SWP 45151	8819.800	52.810±2.112	38.618±1.429	38.881±1.322
SWP 45152	8819.904	41.373±1.655	37.208±1.377	38.237±1.300
SWP 45167	8821.689	39.568±1.583	45.306±1.676	44.545±1.515
SWP 45168	8821.791	48.325±1.933	47.669±1.764	46.635±1.586
SWP 45169	8821.892	51.088±2.044	53.395±1.976	43.804±1.489
SWP 45194	8824.353	50.394±2.016	63.151±2.337	52.316±1.779
SWP 45195	8824.440	61.519±2.461	60.085±2.223	51.566±1.753
SWP 45206	8825.701	60.748±2.430	63.864±2.363	···
SWP 45207	8825.798	66.760±2.670	62.632±2.317	53.268±1.811
SWP 45219	8827.904	67.384±2.695	67.817±2.509	59.430±2.021
SWP 45227	8829.302	69.254±2.770	59.651±2.207	56.059±1.906
SWP 45237	8831.317	70.910±2.836	67.452±2.496	58.335±1.983
SWP 45246	8833.326	72.855±2.914	76.033±2.813	59.754±2.032

[a]Continuum fluxes are given in units of 10^{-15} ergs cm^{-2} s^{-1} Å^{-1}.

Table 3
UV Emission Line Flux Data[a]

Image Name	Julian Date (2,440,000+)	He II λ1640 + O III] λ1663	Si IV λ1400 + O IV] λ1402	Lyα	C IV λ1549	Si III] λ1892 + C III] λ1909
SWP 43438	8611.948	17.051±1.705	12.769±1.430	41.751±1.837	76.614±2.988	9.707±1.175
SWP 43439	8612.031	14.790±1.479	10.856±1.216	41.387±1.821	74.662±2.912	9.180±1.111
SWP 43472	8615.949	15.837±1.584	10.362±1.161	38.720±1.704	69.633±2.716	8.968±1.085
SWP 43473	8616.029	15.365±1.536	11.732±1.314	39.614±1.743	71.235±2.778	13.764±1.665
SWP 43485	8618.118	13.188±1.319	8.559±0.959	37.369±1.644	73.775±2.877	10.270±1.243
SWP 43539	8624.202	14.384±1.438	10.623±1.190	39.431±1.735	66.575±2.596	10.175±1.231
SWP 43540	8624.294	17.992±1.799	9.900±1.109	36.819±1.620	69.660±2.717	13.212±1.599
SWP 43541	8624.385	18.288±1.829	12.007±1.345	39.643±1.744	74.851±2.919	10.466±1.266
SWP 43557	8628.595	18.169±1.817	9.672±1.083	36.259±1.595	65.172±2.542	11.489±1.390
SWP 43587	8631.680	12.129±1.213	9.326±1.045	37.353±1.644	68.481±2.671	11.690±1.414
SWP 43588	8631.765	11.233±1.123	9.692±1.086	35.715±1.571	71.312±2.781	13.907±1.683
SWP 43636	8635.688	13.382±1.338	9.124±1.022	33.320±1.466	64.623±2.520	9.733±1.178
SWP 43676	8639.862	17.282±1.728	10.188±1.141	36.059±1.587	68.877±2.686	10.664±1.290
SWP 43716	8643.948	18.714±1.871	11.037±1.236	40.307±1.774	73.296±2.859	10.240±1.239
SWP 43871	8649.367	13.185±1.319	11.574±1.296	42.142±1.854	72.814±2.840	10.015±1.212
SWP 43872	8649.454	15.884±1.588	12.645±1.416	45.933±2.021	76.959±3.001	10.892±1.318
SWP 43894	8651.756	12.264±1.226	10.932±1.224	38.313±1.686	67.904±2.648	12.443±1.506
SWP 43895	8651.855	14.863±1.486	9.827±1.101	38.525±1.695	67.918±2.649	10.770±1.303
SWP 43921	8656.130	15.008±1.501	9.425±1.056	40.596±1.786	67.940±2.650	8.425±1.019
SWP 43945	8660.040	14.856±1.486	11.559±1.295	39.347±1.731	70.191±2.737	10.595±1.282
SWP 43946	8660.121	13.709±1.371	11.282±1.264	42.857±1.886	68.775±2.682	8.694±1.052
SWP 43962	8664.048	13.022±1.302	11.275±1.263	40.307±1.774	71.699±2.796	10.706±1.295
SWP 43995	8668.022	···	7.140±0.800	35.489±1.562	66.840±2.607	11.294±1.367
SWP 43996	8668.115	···	9.901±1.109	35.812±1.576	69.053±2.693	10.296±1.246
SWP 44020	8672.106	11.764±1.176	10.083±1.129	36.446±1.604	64.753±2.525	9.706±1.174
SWP 44048	8676.272	14.299±1.430	10.509±1.177	35.112±1.545	60.287±2.351	10.137±1.227
SWP 44072	8680.310	11.451±1.145	9.171±1.027	33.214±1.461	65.161±2.541	9.986±1.208
SWP 44099	8684.199	13.925±1.393	10.682±1.196	33.220±1.462	67.461±2.631	11.558±1.399
SWP 44100	8684.275	11.177±1.118	12.329±1.381	31.722±1.396	64.203±2.504	14.211±1.720
SWP 44126	8688.228	8.477±0.848	7.211±0.808	29.611±1.303	57.594±2.246	9.462±1.145
SWP 44149	8692.216	8.912±0.891	7.930±0.888	29.519±1.299	63.911±2.493	9.846±1.191
SWP 44176	8695.910	10.943±1.094	8.069±0.904	26.618±1.171	58.785±2.293	10.981±1.329
SWP 44189	8699.713	8.945±0.894	8.916±0.999	28.493±1.254	57.753±2.252	7.723±0.934
SWP 44208	8703.723	7.663±0.766	8.471±0.949	24.982±1.099	53.504±2.087	8.793±1.064
SWP 44237	8707.871	9.909±0.991	8.974±1.005	27.480±1.209	56.975±2.222	7.860±0.951
SWP 44267	8711.731	13.391±1.339	9.154±1.025	31.722±1.396	60.820±2.372	8.547±1.034
SWP 44307	8715.612	11.593±1.159	12.355±1.384	33.015±1.453	65.884±2.569	9.412±1.139
SWP 44349	8719.932	11.976±1.198	9.588±1.074	33.504±1.474	61.410±2.395	9.790±1.185
SWP 44350	8720.020	15.663±1.566	13.091±1.466	36.571±1.609	67.330±2.626	10.934±1.323
SWP 44381	8724.004	12.488±1.249	8.475±0.949	38.718±1.704	64.045±2.498	9.589±1.160
SWP 44408	8727.967	11.592±1.159	11.942±1.338	39.422±1.735	68.315±2.664	7.924±0.959
SWP 44409	8728.068	···	11.346±1.271	37.210±1.637	67.746±2.642	11.943±1.445
SWP 44410	8728.168	15.773±1.577	11.716±1.312	37.375±1.645	72.573±2.830	11.679±1.413
SWP 44434	8731.946	16.459±1.646	11.614±1.301	41.213±1.813	72.594±2.831	8.378±1.014
SWP 44435	8732.205	···	13.598±1.523	40.652±1.789	68.736±2.681	9.980±1.208
SWP 44461	8735.946	14.037±1.404	10.790±1.208	37.320±1.642	69.492±2.710	11.347±1.373
SWP 44486	8739.990	10.913±1.091	11.056±1.238	33.716±1.484	63.079±2.460	10.973±1.328
SWP 44492	8744.129	10.972±1.097	8.646±0.968	31.276±1.376	63.631±2.482	9.638±1.166
SWP 44581	8747.874	13.851±1.385	10.644±1.192	37.659±1.657	71.354±2.783	9.569±1.158
SWP 44627	8751.845	15.350±1.535	10.311±1.155	34.631±1.524	72.491±2.827	8.062±0.976
SWP 44628	8751.950	14.578±1.458	10.779±1.207	39.274±1.728	71.496±2.788	9.285±1.123
SWP 44629	8752.056	12.920±1.292	8.708±0.975	36.988±1.627	67.524±2.633	9.705±1.174
SWP 44659	8755.872	13.868±1.387	10.749±1.204	37.794±1.663	68.993±2.691	9.236±1.118

Table 3—*Continued*

Image Name	Julian Date (2,440,000+)	He II λ1640 + O III] λ1663	Si IV λ1400 + O IV] λ1402	Lyα	C IV λ1549	Si III] λ1892 + C III] λ1909
SWP 44660	8755.949	···	9.701±1.087	37.884±1.667	71.405±2.785	13.026±1.576
SWP 44682	8759.702	13.730±1.373	11.811±1.323	37.249±1.639	68.033±2.653	7.400±0.895
SWP 44731	8763.559	15.880±1.588	10.974±1.229	36.521±1.607	65.598±2.558	9.866±1.194
SWP 44760	8767.535	10.554±1.055	9.223±1.033	31.337±1.379	54.612±2.130	10.060±1.217
SWP 44803	8771.689	12.725±1.273	11.678±1.308	30.261±1.331	60.436±2.357	9.198±1.113
SWP 44804	8771.772	12.169±1.217	8.260±0.925	30.620±1.347	63.469±2.475	12.367±1.496
SWP 44830	8775.633	15.957±1.596	10.018±1.122	34.556±1.520	61.264±2.389	11.703±1.416
SWP 44873	8779.607	12.230±1.223	13.309±1.491	33.902±1.492	62.857±2.451	7.113±0.861
SWP 44907	8783.948	15.930±1.593	9.829±1.101	35.165±1.547	65.009±2.535	8.760±1.060
SWP 44918	8785.949	10.634±1.063	11.991±1.343	36.745±1.617	62.983±2.456	6.630±0.802
SWP 44921	8787.786	12.702±1.270	10.055±1.126	34.865±1.534	64.779±2.526	10.548±1.276
SWP 44922	8787.864	11.840±1.184	8.687±0.973	34.194±1.505	66.079±2.577	11.881±1.438
SWP 44935	8790.113	14.784±1.478	9.681±1.084	33.982±1.495	67.992±2.652	11.232±1.359
SWP 44949	8791.769	15.495±1.549	11.760±1.317	37.262±1.640	70.532±2.751	9.822±1.188
SWP 44950	8791.857	15.004±1.500	10.425±1.168	36.716±1.616	67.412±2.629	14.068±1.702
SWP 44964	8793.963	14.658±1.466	9.572±1.072	37.016±1.629	67.780±2.643	10.045±1.215
SWP 44974	8795.768	14.577±1.458	10.878±1.218	37.405±1.646	69.919±2.727	8.464±1.024
SWP 44992	8797.448	16.789±1.679	11.013±1.233	37.606±1.655	71.690±2.796	11.005±1.332
SWP 44993	8797.538	15.144±1.514	10.938±1.225	37.047±1.630	71.722±2.797	10.318±1.248
SWP 45010	8799.460	15.066±1.507	10.861±1.216	38.602±1.698	61.098±2.383	9.052±1.095
SWP 45024	8801.764	11.581±1.158	11.610±1.300	···	63.585±2.480	11.248±1.361
SWP 45025	8801.887	13.310±1.331	9.372±1.050	34.032±1.497	64.283±2.507	10.079±1.220
SWP 45026	8801.996	11.679±1.168	9.878±1.106	35.559±1.565	64.598±2.519	11.732±1.420
SWP 45038	8803.458	11.433±1.143	11.278±1.263	36.813±1.620	66.819±2.606	8.374±1.013
SWP 45052	8805.543	16.844±1.684	12.541±1.405	41.348±1.819	73.452±2.865	10.795±1.306
SWP 45063	8807.520	16.108±1.611	13.618±1.525	40.783±1.794	72.034±2.809	11.587±1.402
SWP 45064	8807.603	15.292±1.529	12.634±1.415	36.449±1.604	72.370±2.822	12.714±1.538
SWP 45081	8809.509	14.375±1.438	12.532±1.404	35.314±1.554	70.550±2.751	11.009±1.332
SWP 45082	8809.601	14.549±1.455	13.052±1.462	38.033±1.673	74.732±2.915	9.878±1.195
SWP 45096	8811.493	15.791±1.579	13.392±1.500	35.964±1.582	69.099±2.695	11.158±1.350
SWP 45097	8811.595	15.899±1.590	13.384±1.499	38.451±1.692	72.306±2.820	10.461±1.266
SWP 45106	8813.384	14.546±1.455	10.726±1.201	36.440±1.603	64.005±2.496	12.925±1.564
SWP 45118	8816.028	13.700±1.370	8.430±0.944	34.493±1.518	67.487±2.632	11.906±1.441
SWP 45133	8818.024	10.933±1.093	11.187±1.253	32.175±1.416	66.611±2.598	11.225±1.358
SWP 45150	8819.700	8.954±0.895	8.490±0.951	27.355±1.204	55.596±2.168	···
SWP 45151	8819.800	7.794±0.779	6.574±0.736	31.274±1.376	52.838±2.061	12.267±1.484
SWP 45152	8819.904	7.073±0.707	8.813±0.987	30.107±1.325	59.321±2.314	9.929±1.201
SWP 45167	8821.689	11.037±1.104	8.706±0.975	30.555±1.344	62.589±2.441	10.167±1.230
SWP 45168	8821.791	12.697±1.270	7.656±0.857	29.693±1.306	57.353±2.237	9.218±1.115
SWP 45169	8821.892	11.109±1.111	8.925±1.000	29.510±1.298	56.358±2.198	11.512±1.393
SWP 45194	8824.353	14.707±1.471	9.936±1.113	31.339±1.379	59.284±2.312	8.923±1.080
SWP 45195	8824.440	13.914±1.391	···	29.242±1.287	61.297±2.391	9.275±1.122
SWP 45206	8825.701	14.222±1.422	10.173±1.139	33.615±1.479	64.641±2.521	···
SWP 45207	8825.798	16.205±1.620	9.322±1.044	30.904±1.360	60.589±2.363	10.583±1.281
SWP 45219	8827.904	14.897±1.490	12.322±1.380	35.942±1.581	63.532±2.478	8.180±0.990
SWP 45227	8829.302	14.370±1.437	14.745±1.651	36.139±1.590	72.627±2.832	9.507±1.150
SWP 45237	8831.317	14.427±1.443	13.534±1.516	35.966±1.583	66.867±2.608	9.803±1.186
SWP 45246	8833.326	18.615±1.862	11.108±1.244	36.969±1.627	69.398±2.707	11.312±1.369

[a]Emission line fluxes are in units of 10^{-13} ergs cm^{-2} s^{-1}.

Table 4
UV Velocity Data[a]

Emission Line	V_{FWHM}^{rest}(rms)	V_{FWHM}^{rest}(mean)
He II λ1640 + O III] λ1663	6.34±0.90	4.74±0.69
Si IV λ1400 + O IV] λ1402	5.73±2.71	4.81±0.50
Lyα	...	...
C IV λ1549	3.55±0.59	3.03±0.07
Si III] λ1892 + C III] λ1909	2.61±0.16	2.82±0.31

[a]Velocity data are in units of 10^3 km s^{-1}.

Table 5

Optical Flux Data

Image Name	Julian Date (2,440,000+)	F(λ5150)[a]	Hβ[b]
n38607a	8607.830	11.406±0.605	9.829±0.403
n38623a	8623.830	11.707±0.620	10.100±0.414
n38627a	8627.830	11.094±0.588	10.272±0.421
n38631a	8631.840	10.865±0.576	10.494±0.430
n38635a	8635.830	10.781±0.571	10.183±0.418
n38639a	8639.840	11.303±0.599	10.327±0.423
n38643a	8643.720	12.788±0.678	10.423±0.427
n38647a	8647.760	12.668±0.671	10.459±0.429
n38651a	8651.670	11.190±0.593	10.603±0.435
n38656a	8656.770	12.163±0.645	10.669±0.437
n38660a	8660.770	11.629±0.616	10.109±0.414
n38664a	8664.770	11.005±0.583	10.894±0.447
n38668a	8668.810	10.204±0.541	10.969±0.450
n38676a	8676.710	10.817±0.573	9.760±0.400
n38677a	8677.800	10.786±0.572	9.483±0.389
n38678a	8678.680	10.703±0.567	9.513±0.390
n38704a	8704.580	8.763±0.464	8.469±0.347
n38712a	8712.590	10.350±0.549	8.410±0.345
n38716a	8716.600	10.055±0.533	8.840±0.362
n38720a	8720.590	11.842±0.628	9.395±0.385
n38724a	8724.560	11.257±0.597	9.640±0.395
n38732a	8732.560	11.212±0.594	9.357±0.384
n38736a	8736.550	10.149±0.538	9.410±0.386
n38744a	8744.610	10.812±0.573	10.537±0.432
n38752a	8752.570	11.174±0.592	9.606±0.394
n38763a	8763.580	11.880±0.630	11.678±0.479
n38764a	8764.560	10.754±0.570	10.131±0.415
n38772a	8772.630	11.799±0.625	9.627±0.395
n38776a	8776.560	10.636±0.564	9.272±0.380
n38794a	8794.570	11.444±0.607	10.803±0.443
n38804a	8804.470	12.281±0.651	11.780±0.483
n38808a	8808.480	12.773±0.677	10.531±0.432
n38822a	8822.480	12.917±0.685	11.060±0.453
n38824a	8824.470	11.765±0.624	10.108±0.414
n38826a	8826.470	12.717±0.674	9.912±0.406
n38830a	8830.480	12.108±0.642	11.026±0.452
n38832a	8832.460	13.281±0.704	11.086±0.455

[a]Continuum fluxes are in units of 10^{-15} ergs cm^{-2} s^{-1} Å^{-1}.

[b]Emission line fluxes are in units of 10^{-13} ergs cm^{-2} s^{-1}.

Table 6
Sampling Statistics

Subset	Number	Sampling Interval (days) Average	Median	F_{var}	R_{max}	Reference
Previous 1460 Å continuum dataset	69	3.3	3.9	0.201	3.027±0.380	1
New UV dataset; binned by epoch	69	3.3	3.9	0.203	3.119±0.163	
New UV dataset; complete sample	101	2.2	2.0	0.192	2.856±0.162	
New UV dataset; 4-day sampling period	62	2.8	3.9	0.193	2.762±0.145	
New UV dataset; 2-day sampling period	40	1.3	1.7	0.140	2.043±0.107	
Previous 5150 Å continuum dataset	72	3.2	2.0	0.078	1.517±0.042	2
New optical dataset; binned by epoch	35	6.6	4.0	0.065	1.516±0.114	
New optical dataset; complete sample	37	6.2	4.0	0.064	1.516±0.114	

References.—(1) Reichert et al. 1994; (2) Stirpe et al. 1994.

Note.—Previously published light curves were collected from the AGN Watch website.

Table 7

Cross-Correlation Results[a]

Line/Band	Previous Results[b] τ_{cent}^{rest}	Previous Results[b] τ_{peak}^{rest}	Current Results τ_{cent}^{rest}	Current Results τ_{peak}^{rest}
F(λ1460)	...	...	$-0.1_{-0.2}^{+0.3}$	$0.0_{-0.4}^{+0.2}$
F(λ1835)	0.1_{-3}^{+3}	0_{-2}^{+2}	$0.0_{-0.3}^{+0.3}$	$0.0_{-0.5}^{+0.6}$
F(λ5150)	1.6_{-2}^{+2}	1_{-2}^{+2}	$0.4_{-1.6}^{+3.1}$	$0.7_{-1.6}^{+1.9}$
He II λ1640 + O III] λ1663	0.5_{-4}^{+4}	1_{-2}^{+2}	$1.3_{-0.5}^{+0.9}$	$1.4_{-1.1}^{+0.6}$
Si IV λ1400 + O IV] λ1402	3.9_{-4}^{+4}	5_{-2}^{+2}	$2.1_{-1.5}^{+0.9}$	$2.3_{-2.4}^{+0.8}$
Lyα	3.8_{-3}^{+3}	4_{-2}^{+2}	$3.6_{-0.7}^{+1.1}$	$2.2_{-0.1}^{+2.5}$
C IV λ1549	5.4_{-3}^{+3}	5_{-2}^{+2}	$3.8_{-0.9}^{+1.0}$	$4.5_{-2.2}^{+0.4}$
Si III] λ1892 + C III] λ1909[c]	15.6_{-4}^{+4}	9_{-2}^{+2}	$8.5_{-2.6}^{+1.3}$	$10.2_{-5.3}^{+0.2}$
Hβ	7.1_{-2}^{+2}	8_{-2}^{+2}	$10.4_{-2.3}^{+4.1}$	$9.0_{-2.4}^{+5.1}$

[a]All time lag data are in units of days.

[b]The previous results listed here are adapted from the GEX-extracted UV data of Reichert et al. (1994) and from the optical results of Stirpe et al. (1994), both of which used the 1460 Å continuum as the driving light curve.

[c]The range of time lags we included in our analysis of Si III] λ1892 + C III] λ1909 was limited to $\pm$16 days to avoid aliasing.